

Processing Effects on the Friction Stir Weld Stir Zone

This investigation attempts to understand the true temperature at the workpiece/weld tool interface

BY J. SCHNEIDER, R. STROMBERG, P. SCHILLING, B. CAO, W. ZHOU, J. MORFA, and O. MYERS

ABSTRACT

While many researchers have carefully mapped out the various microstructural regions of a friction stir weld (FSW), concluding that each region undergoes different thermomechanical cycles during the process, these studies generally have only considered one set of FSW parameters. By considering only the shear zone (SZ) over a range of FSW process parameters, it can be observed that material within this region is also subjected to different thermomechanical cycles. Whether this results from a temperature increase with higher rev/min and/or material held for an increased time at temperature, is still not understood. This study, however, does give insight into the often conflicting results published regarding the microstructural evolution in a FSW.

Introduction

As with most welding processes, friction stir welding (FSW) produces a non-homogenous macrostructure whose regions, illustrated in Fig. 1, include the heat-affected zone (HAZ), thermomechanical-affected zone (TMAZ), and weld nugget or stir zone (SZ). Each zone is characterized by a unique microstructure related to different levels of thermomechanical processing. The tool rotation and travel impart a nonsymmetrical flow pattern that is observed in the nonsymmetric weld structure of the transverse section in Fig. 1. The side where the tool rotation and travel vectors are in the same direction is labeled the advancing side (AS), and where they are opposed is labeled the retreating side (RS). Because FSW is a solid-state process, correlation of the temperature at the workpiece/weld tool interface with the processing parameters presents challenges. Understanding of this correlation is needed for control of the processing temperature and optimization of the resulting mechanical properties.

Because the maximum temperature in FSW is generally considered to be at the shear interface between the SZ and the TMAZ (Refs. 1–3), understanding the variation in temperature in this region

with respect to processing parameters is necessary. Numerous studies report the resulting weld temperature to be most strongly influenced by the tool rotation velocity (Refs. 2–7). In addition to understanding the temperature, the heating rate can also affect the kinetics of the phase changes in age-hardenable alloys such as the AA2xxx series. Since the FSW process is considered to involve a large shear strain at high rates (Refs. 2, 8–12), the heating or up-quenching times associated with the process may be very rapid (Ref. 13).

Determining the temperature at the workpiece/weld tool interface was directly approached using embedded thermocouples in 2xxx series aluminum alloys (Refs. 1, 2, 14–20), and it has provided information on the relative homologous temperature in the range of 0.80 to 0.90 T_m (where T_m is the melting temperature of the Al with a value of 933 K). Little variance has been reported with SZ temperature measurements of 525°C in AA2024 (Ref. 17) and 480°–520°C in AA2195 (Ref. 14), where the increase in temperature corresponded to an increase in tool rotation. Positioning the thermocouple close to the shear zone has noted difficulties due to

potential displacement by the resulting material flow and response to rapid heating conditions. Thus, most thermocouple measurements have been used to validate a numerical model with extrapolation of measured temperatures outside the SZ to the workpiece/weld tool interface. Attempts to model the temperature in the shear region have often resulted in over-prediction of the weld temperature, which has been attributed to slippage occurring at the workpiece/weld tool interface (Refs. 21, 22). While relationships between peak temperature and processing conditions have been shown (Refs. 2, 14), they are not considered to change the overall temperature field significantly (Ref. 22).

Conversion of weld power to thermal energy has also been pursued to determine the weld temperature (Refs. 23–27), and may have validity if the temperature does not exceed the eutectic or solidus temperature resulting in tool slippage and reduced efficiency (Refs. 13, 21).

Since the processing temperature controls the resulting mechanical properties, as affected by microstructural variations, interpretation of the resulting grain size and precipitate state can be used to verify processing temperatures and provide insight as to the heating conditions, and hence, strain rate experienced during FSW of age-hardenable alloys (Refs. 8–10, 12, 13, 28). Due to the complex nature of the FSW process, various characterization methods at different length scales are often needed to interpret the results. Although much research has been published on the resulting microstructure and mechanical properties of FSW in the age-hardenable 2xxx series (Refs. 14, 15, 19, 20, 27–39), these studies generally characterized a single FSW obtained with a single set of processing parameters that covered a range of tool rotations from 120 to 1040 rev/min. Further adding to the difficulty of comparing findings, not all studies document details of the tool design and processing parameters. Thus, assessing whether the microstructural evolution observed is due to the material, tool design, processing parameters, or some combination is difficult and sometimes results in conflicting findings. Studies on 2024 (Refs.

KEYWORDS

Aluminum
Friction Stir Welding
Heat-Affected Zone
Shear Zone
Solid-State Welding

J. SCHNEIDER, J. MORFA, and O. MYERS are with Mechanical Engineering Department, Mississippi State University, Mississippi State, Miss. R. STROMBERG is with Hysitron, Inc., Minneapolis, Minn. P. SCHILLING is with Mechanical Engineering Department, University of New Orleans, New Orleans, La. B. CAO and W. ZHOU are with Advanced Materials Research Institute, University of New Orleans, New Orleans, La.

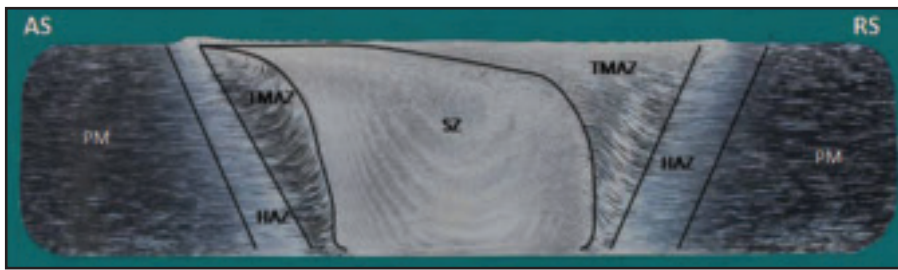


Fig. 1 — Transverse view of a conventional friction stir weld with regions of interest labeled.

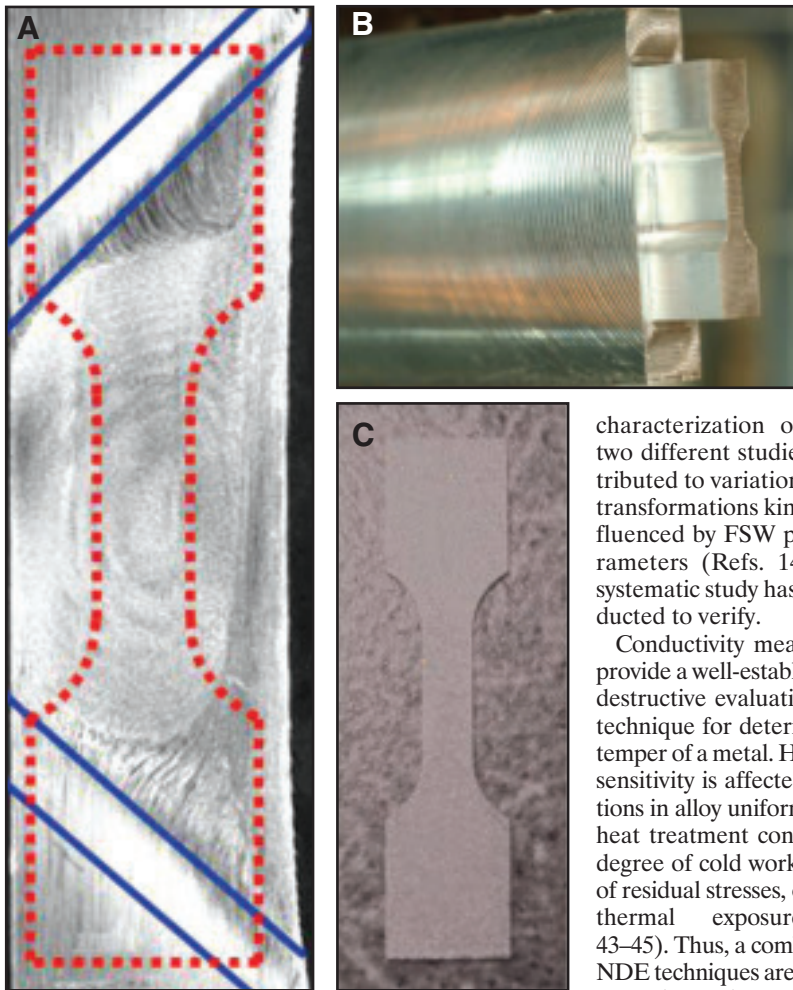


Fig. 2 — Miniature tensile specimens fabricated from the FSW nuggets. A — Shown are the specimens from the FSW transverse microstructure with the specimen geometry superimposed; B — an end mill was used to machine the dogbone geometry; C — which was then sliced into individual specimens using wire EDM.

19, 30, 33–35) report a range of complex precipitate morphologies in the SZ with coarse particles dissolving providing solute for postweld natural aging. In contrast, studies on 2219 report either particle coarsening (Refs. 36–38, 40) and/or the dissolution of the Al_2Cu phase in the SZ (Refs. 15, 20). Nonhomogeneities observed at the macroscale have been attributed to banding of large constituent particles, which correspond to tool rotation variations in 2024 (Refs. 41, 42), different tempers of 2219 (Ref. 36), or overpass repair welds in 2219 (Ref. 38). While differences in the microstructural

characterization of 2195 in two different studies were attributed to variations in phase transformations kinetics as influenced by FSW process parameters (Refs. 14, 31), no systematic study has been conducted to verify.

Conductivity measurements provide a well-established non-destructive evaluation (NDE) technique for determining the temper of a metal. However, its sensitivity is affected by variations in alloy uniformity due to heat treatment condition, the degree of cold work, presence of residual stresses, or effect of thermal exposure (Refs. 43–45). Thus, a combination of NDE techniques are often used to evaluate the temper of an alloy such as combining eddy current with hardness testing. While these standard techniques are typically used at the macroscale where homogeneity of the thermomechanical processing is assumed, characterization at the microscale can provide insight into nonhomogenous variations.

This study evaluated the combined use of conductivity measurements with hardness testing at the macro and micro length scales to evaluate the resulting microstructure in a FSW SZ formed by varying the tool rotation. The range of tool rotations in the study was selected based on earlier studies where a large change in the resulting SZ strength was observed (Ref. 46). Microstructural features were correlated with conductivity and hardness

measurements. The results in this study were also compared with temperature calculations based on conversion of weld power to thermal energy (Ref. 27).

Experimental Procedure

Friction stir welds were made in rolled panels of aluminum alloy 2219-T87 approximately 610 mm long, 152 mm wide, and 6.4 mm thick that were butted together. Nominal composition of the 2219 alloy (wt-%) is Cu 6.30%, Mn 0.30%, Zr 0.17%, V 0.10%, Ti 0.06%, Fe 0.15%, Si 0.10%, and balance Al. The FSW tool consisted of a 12.7-mm-diameter UNF left-handed pin, a 30.5-mm-diameter scrolled shoulder, and a pin length of approximately 6.2 mm. All FSWs were performed with a zero degree lead angle and in-position control. A RM-1 model FSW machine from Manufacturing Technology, Inc. (MTI), was used to produce the welds with the data recorded using a high-speed National Instruments Data Acquisition system.

Metallographic specimens were taken of the transverse section of each FSW segment. The specimens were mounted and polished using standard metallurgical procedures. All samples were etched using Keller's reagent to document the macrostructure as recorded with a Nikon D1 camera. Surface topography was obtained in a scanning probe microscopy (SPM) using a diamond Berkovich probe mounted on the Hysitron TI 950™. Prior to SPM, the specimens were mechanically reground and repolished using 1.0- and 0.5-micron alumina on the pad followed by colloidal silica.

Indentation experiments were conducted using the Hysitron TI 950™ instrument equipped with the nanoECR™ (electrical contact resistance) package and a conductive boron-doped diamond Berkovich probe with a tip radius of approximately 150 nm. The nanohardness of each transverse specimen was measured across the width approximately 1.3 mm below the crown surface. One hundred indents with a spacing of 250 μm were made using a 5-s loading to a peak of 10 mN, 5-s hold, and 5-s unloading segments, which corresponded to an average indentation contact depth of 485 nm.

To measure the nanoconductivity, the nanoECR™ package was used, which enables simultaneous electrical measurements to be made during standard nanoindentation testing. During testing, a fixed voltage was applied to the sample via a conducting stage and the resultant current flow through the sample was measured through the conducting tip. Voltage was held constant at 2 V and the measured current was used to calculate the average current density based on the contact area of the indenter at peak loading.

Bulk eddy current measurements were made with Rohmann GmbH Elotest M2 with a probe diameter of approximately 1.3 cm, which was operated at a frequency of approximately 1 MHz. The values were recorded as % IACS, where the electrical conductivity of annealed Cu was referenced as 100% IACS at 20°C, and IACS refers to the International Annealed Copper Standard, which was established in 1913 (Ref. 47). Advertised accuracy of measurements was $\pm 0.1\%$ IACS. Because the probe diameter was larger than the weld cross section, some air was picked up. Although this may have resulted in slightly lower values for % IACS, the comparative trend was considered valid.

To evaluate the mechanical properties of only the SZ of the FSW, tensile specimens were designed with the gauge section entirely within the transverse section of the FSW SZ, as shown in Fig. 2A. The geometry was first machined, and then sliced using wire electrical discharge machining (EDM) into individual specimens 2.0 cm long \times 0.64 cm wide \times 0.03 cm thick, as shown in Fig. 2B and C, respectively. The tensile specimens were tested in uniaxial tension using a stepper-motor-driven miniature tensile tester with a 0.5-kN (100-lbf) load cell. All tests were run at ambient temperature at a constant crosshead velocity of 0.05 mm/min with a data-acquisition rate of 1 sample per s. The maximum load (F_{max}) was divided by the initial specimen cross-sectional area (A) to calculate the engineering stress (σ). Yield strength (σ_{YS}) was defined using the 0.02% offset criteria (Ref. 48) and ultimate tensile strength (UTS) was defined using the maximum load carried by the specimen cross-sectional area.

A JEOL 6500 F field emission, scanning electron microscope (FE-SEM) with an Oxford electron backscatter detector (EBSD) was used to obtain orientation image maps (OIM) of the SZ. Analysis was performed in 0.4- μ m steps over 215- \times 161- μ m rectangular areas in the banded regions of the transverse sections. All OIM scans were obtained using an excitation condition of 20 kV with a working distance of 20 mm. EBSD/OIM was used to determine grain size based on a 5-deg misorientation angle.

Transmission electron microscope (TEM) foils, 3 mm in diameter, were punched from the SZ region of the FSW specimens and were prepared for imaging using traditional techniques of mechanical thinning, two-sided dimpling, and ion milling to electron transparency. Initial images were obtained in a JEOL JEM-100CX TEM with a tungsten filament operated at an accelerating voltage of 100 kV to obtain bright field image (BFI). Complementary higher-resolution BFIs and selected area diffraction (SAD) patterns

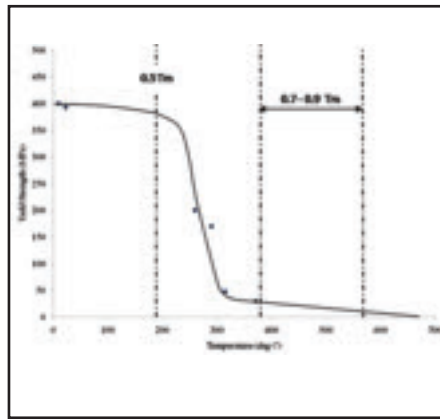


Fig. 3 — Flow stress of 2219-T87 vs. temperature showing a precipitous drop at $0.5T_m$ before reaching an almost constant, linear plateau in the range of 0.7 to $0.9 T_m$ (Ref. 50).

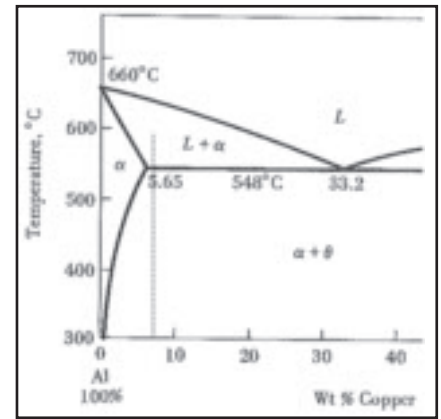


Fig. 4 — Phase diagram for the Al-Cu binary system (Ref. 51).

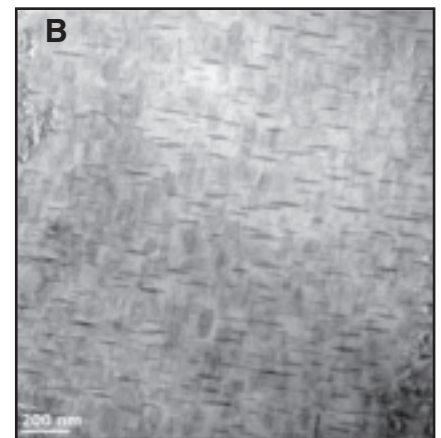
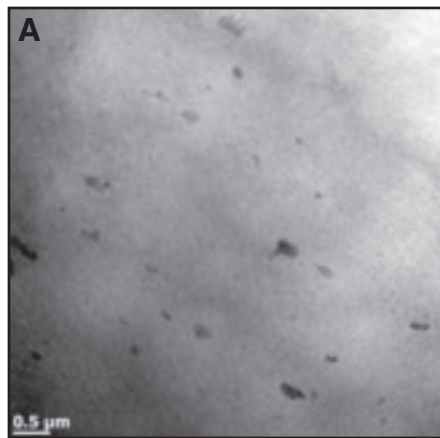


Fig. 5 — A — A low-magnification image of the base metal in which a few large overaged particles (200–500 nm) can be observed; B — the higher-magnification image shows the θ' strengthening phases in the base metal matrix.

were obtained using a JEOL 2010 200 KeV field emission (FE) TEM.

A Rigaku Smartlab X-ray diffractometer (XRD) with Cu-k X-ray was used to identify the minor phases present in the aluminum matrix. A continuous scan was made at a rate of 0.035 deg/min over a 2- θ range of 18 to 55 deg.

The SZ temperature was taken to be that of the workpiece/weld tool interface or the shear zone. The shear zone temperature was calculated from the measured experimental torque values using an alternative heat index (Ref. 27). This numerical approach considered the power generated by rotating an axial symmetric

Table 1 — Summary of FSW Conditions and Corresponding Shear Strain Rate

RPM	Tool Radius (mm)	Shear Zone Thickness (mm)	Shear Strain Rate (s^{-1})
150	6.35	0.13	5×10^4
200	6.35	0.13	6×10^4
300	6.35	0.13	9×10^4

Table 2 — Grain Size as Inferred from EBSD/OIM

Specimen	Grain Size (μ m)	
	AS	RS
150	2.5	1.8
200	2.8	2.6
300	4.1	4.2

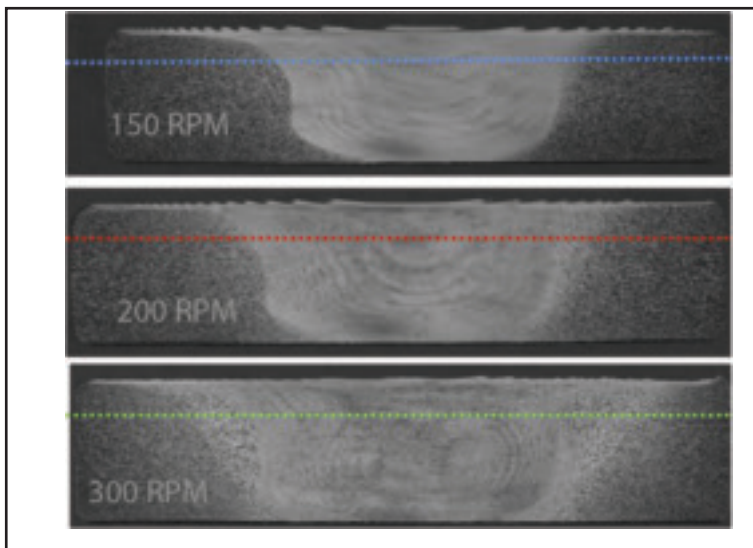


Fig. 6 — Macrographs of the FSWs in this study with horizontal line indicating location of nanoindentations.

plug of metal around the tool. By assuming that 100% of the weld torque was converted into thermal energy and contact conditions remain constant, an energy balance was used to equate the heat input (Q_g) with the heat loss terms as given in Equation 1. The heat loss terms included conduction, through the weldment (Q_w), anvil (Q_a), and spindle (Q_{sp}), in addition to convection, which captured the pre-heating of metal (Q_v) passing through the shear surface in advance of the weld.

$$Q_g = Q_w + Q_a + Q_{sp} + Q_v \quad (1)$$

The resulting relationship given in Equation 2 was used to determine a FSW temperature from the actual weld torque (M_t) (Refs. 27, 49) where ω was the tool rotation, τ was the flow stress, R_s was the radius of shear surface, R was the radius of the tool pin, and H was the length of the tool pin.

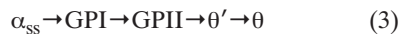
$$Q_g = \omega\tau 2\pi R^3 \left[\frac{1}{3} \left(\frac{R_s}{R} \right)^3 + \frac{H}{R} \right] \quad (2)$$

The flow stress (τ) was approximated by $M_t^* \Delta T$ such that as the shear zone temperature approached T_m , the flow stress approaches zero (Refs. 27, 49). This linear approximation was based on Fig. 3, which plots the flow stress vs. temperature for AA2219-T87 7 and shows a precipitous drop

at around $0.5 T_m$ reaching a constant, linear plateau at approximately $0.7 T_m$ (Ref. 50). The value of flow stress at T_m was assumed to be zero. Thus, considering the range of published temperature measurements for FSW Al alloys of 0.8 to $0.9 T_m$, the corresponding flow stress was relatively unaffected by temperature and was considered linear just prior to reaching T_m .

Results and Discussion

AA2219 is an Al-Cu alloy whose nominal composition is slightly above the maximum solid solubility as shown in the equilibrium diagram in Fig. 4 (Ref. 51). This yields a microstructure composed primarily of the saturated α -aluminum matrix plus a small amount of excess θ phase. The T87 temper used in this study refers to a heat treatment that artificially ages the Cu-rich precipitates in the α -matrix through a well-accepted sequence of equilibrium transformation given in Equation 3, where α_{ss} refers to a solid solutionized Al matrix.



The T8 temper refers to a solid-solution heat treatment of the α phase at 535°C , followed by cold work and artificial aging at 175°C for 18 h (Ref. 52). This results in a base metal with the main strengthening

metastable phase of θ' phase as shown in Fig. 5. Figure 5A is a low-magnification image of the base material microstructure, which shows a few large Cu-rich particles around 200–500 nm, corresponding to the excess θ phase. Figure 5B is a higher magnification image that shows the θ' strengthening metastable phase with a reported morphology of tetragonal discs that are semicoherent with the α -aluminum matrix (Ref. 53).

The FSW process is considered to occur at high strain rates and impart a high strain to the metal surrounding the weld tool (Refs. 2, 8–12). Thus, the kinetics of the dynamic microstructural evolution would be expected to differ from the static equilibrium conditions (Refs. 13, 19). The occurrence of a high strain rate acting on the metal as it moves around the weld tool implies very rapid deformational heating and associated up-quenching followed by slow cooling. The strengthening precipitates in the base metal undergo coarsening during the FSW process and eventually lose their strengthening effectiveness due to elevated temperatures and/or longer times at elevated temperatures.

Near the workpiece/weld tool interface, where the rate of heating was the highest due to the high shear strain rates, the Cu-rich phases underwent dissolution. During the rapid up-quenching, if the eutectic temperature was exceeded at the workpiece/weld tool interface, the remaining θ phase may have liquated (Refs. 13, 54). However, if the temperature remained below the eutectic, an increasing degree of dissolution of the Cu-rich phases was expected as the rate of temperature rise increased at the workpiece/weld tool interface, thereby increasing the solute concentration. At lower strain rate regions away from the shear zone, the Cu-rich phases would have continued to coarsen, depleting the solute from the α matrix (Ref. 19).

Estimations of the strain rate associated with FSW have been based on various analytical or numerical models that rely on material property databases (Refs. 8–11) in addition to use of the Zener-Holloman parameter, which relates grain size to strain rate (Ref. 12). These methods have provided estimates in the range of 10^4 to 10^1 s^{-1} , respectively, with lower values calculated from the Zener-Holloman method. Studies have indicated that the grain size at

Table 3 — Tensile Strength of the FSW SZ Specimens

Specimen	Yield Strength (MPa)	Ultimate Tensile Strength (MPa)
150	151 ± 2	269 ± 11
200	163 ± 11	295 ± 11
300	190 ± 2	332 ± 9
PM	396	469

Table 4 — Bulk Eddy Current Measurements

Specimen	Eddy Current (% IACS)
150	26.2 ± 0.1
200	26.2 ± 0.7
300	22.7 ± 0.1

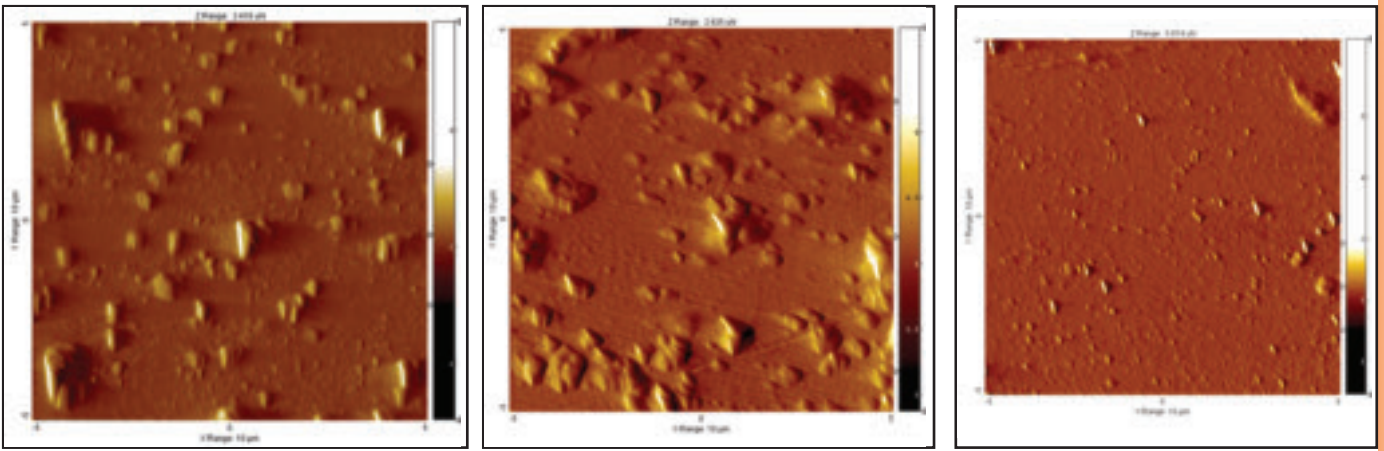


Fig. 7 — SPM images show higher amounts of precipitates on the surfaces of the FSWs made at A — 150 rev/min; B — 200 rev/min; than on the C — 300 rev/min sample surface.

the workpiece/weld tool interface are smaller than in the FSW wake, which has been attributed to grain growth during the slow cooling of the workpiece (Ref. 55). As grain sizes have been reported to increase with increasing tool rotation due to post-weld grain growth, use of the Zener-Hollomon method results in an underestimation of the strain rate. The highest shear strain rate has been estimated based on a kinematic approach that does not rely on an assumption of material properties at the FSW conditions (Refs. 11, 49). Using this approach, an estimate of the mean shearing strain rate ($\dot{\gamma}$) across the shear surface of thickness (δ) at the workpiece/weld tool interface has been made using Equation 4 (Ref. 11).

$$\dot{\gamma} \cong \frac{(r \cdot \omega)}{\delta} \quad (4)$$

In Equation 4, r is the radius of the shear surface approximated by the pin tool radius and ω is the angular velocity of the metal inside the shear surface taken to be approximately the same as that of the tool. The shear zone thickness, δ , is estimated to be on the order of 0.1 times the pin diameter (Refs. 1, 3, 46, 49). The estimated shear strain rates are summarized in Table 1 showing increasing rates as the tool rotation increases. As the travel speed was constant in this study at 114 mm/min, the higher strain rate corresponded to a faster heating rate at the shear surface surrounding the SZ. Note that this was an instantaneous shear strain rate that the material experienced as it crossed the shear zone. Neighboring material adjacent to the shear zone experienced less shearing, and hence, lower temperatures. The intertwining of these two flow paths in the SZ region was reported to result in the shear textures or onion ring pattern observed in the FSW SZ (Refs. 56, 57)

Macrographs of the etched transverse sections of the three welds are shown in Fig. 6. They were repolished to obtain the

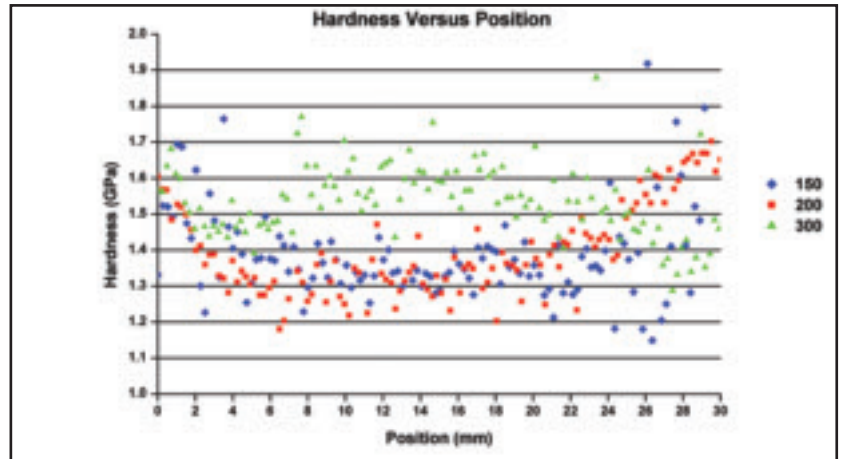


Fig. 8 — Nanohardness measurements on FSW samples showing higher hardness at 300 rev/min due to natural aging.

SPM surface profiles shown in Fig. 7. Preferential polishing around the harder Cu-rich particles reveal an increasing number as the rotation is increased from 150 to 200 rev/min. However, at 300 rev/min, a decrease in the average size and the volume fraction of hard Cu-rich particles assumed to be the θ phase was observed. This would correspond to an increased dissolution rate of the θ phase as the rev/min, and hence the strain rate, increased above a critical level.

The representative grain size measurements for the three FSWs in this study were obtained using electron backscattered diffraction (EBSD)/orientation image mapping (OIM). Table 2 summarizes the variation in grain size observed between the AS and RS of the FSWs. The larger, more uniform grain size in the 300 rev/min FSW specimen was consistent with exposure to higher temperatures or longer cooling times for the workpiece, similar to other reports (Refs. 39, 55). Thus, the higher SZ strength at the higher revs/min cannot be attributed to Hall-Petch strengthening, but rather to the precipitate state.

The horizontal dashed line, shown on the macrographs in Fig. 6, indicate the lo-

cation of the nanoindentations summarized in Fig. 8. While a reduction in hardness was observed for the welds made at 150 and 200 rev/min, the 300 rev/min FSW had a higher value. Table 3 lists a comparison of the FSW strengths to the base metal. Although all FSWs had a lower strength than the base metal, a trend toward increased tensile strength was noted for the SZ as the tool rotation increased. Estimating a weld temperature based on conversion of power to heat, assuming a 100% efficiency and constant contact conditions, predicted a higher temperature at the higher tool rotation. For natural aging to occur, Cu-rich phases in the 2219-T87 material would have to dissolve and increase the amount of solute in the α -matrix in the wake of the FSW. TEM images indicated that the θ phase was dissolved, thus replenishing the solute in the α phase for postweld natural aging.

On the basis of the hardness data and corresponding SPM images, there was a significant change in either the localized temperature or the heating rate between the FSWs made at 300 rev/min and the 150 and 200 rev/min. There was no evidence of exceeding the eutectic temperature, either by

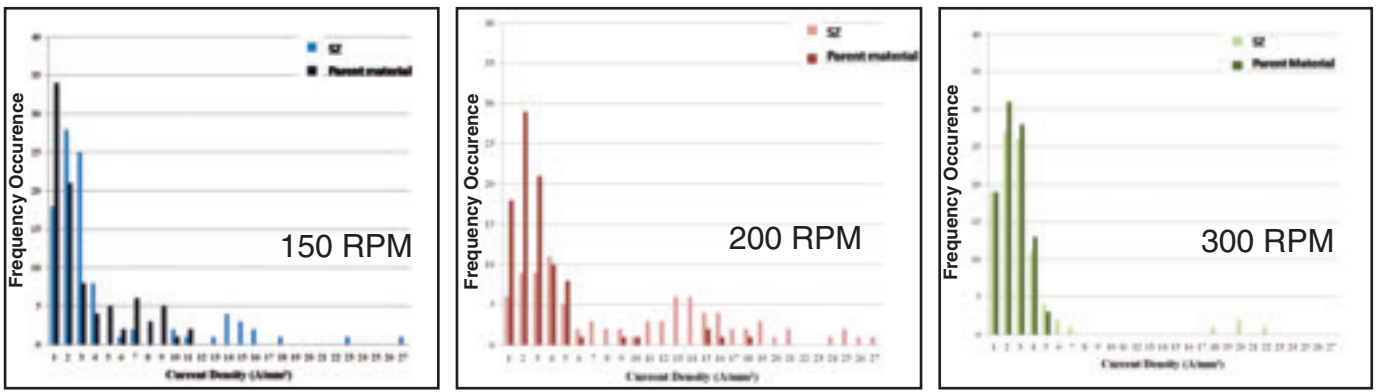


Fig. 9 — Histograms of current density from indents performed within the weld nugget and at the outer edge of each sample. High current density “outliers” are linked to the presence of Cu-rich precipitates.

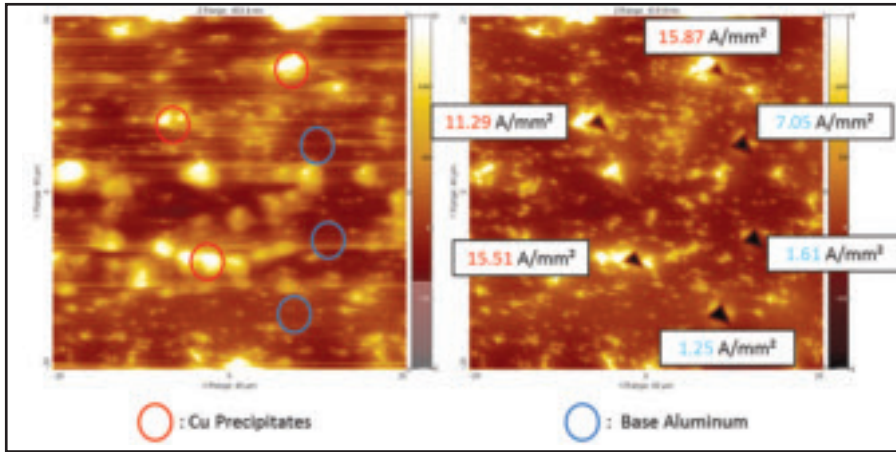


Fig. 10 — Piezo-automation results confirming higher current density for indents placed on Cu-rich precipitates.

Table 5 — FSW Temperatures Calculated Using the Alternative Heat Index

Specimen	Calculated Temperature (°C)
150	523
200	532
300	542

To understand this variation, individual current density measurements were made directly on the Cu-rich particles and compared with the Al matrix as shown in Fig. 10. As can be observed, a higher current density range of 11–16 A/mm² was associated with the large Cu-rich particles, with a lower current density range of 1–7 A/mm² was associated with the matrix. Thus, the histograms can be interpreted as the 150 and 200 rev/min FSWs having a higher concentration of larger Cu-rich particles in the SZ than in the 300 rev/min FSW. This corresponded with the decrease in eddy current measurements as the volume fraction of large Cu-rich particles decreased. This was also consistent with predominant coarsening of the θ phase at lower revs/min and greater dissolution at the higher revs/min.

To investigate the details of the precipitate state, TEM images were obtained as summarized in Figs. 11–13 for FSWs at 150, 200, and 300 rev/min respectively. At 150 and 200 rev/min, a mixed precipitate state was observed, which included a range of large Cu-rich precipitates that were identified as CuAl₂ or θ phase. Smaller θ' disc-shaped strengthening precipitates, ranging from 20–50 nm, were also observed in Fig. 11, which coarsen to 50 to 150 nm in Fig. 12. In Fig. 13, for the 300 rev/min specimen, a more uniform coarsening of the smaller θ' precipitates was observed, which was also observed in the superlattice reflections in the accompanying SAD pattern of Fig. 13C due to increased volume fraction (Ref. 20). The microstructure of the 300 rev/min specimen showed almost none of the larger overaged phase or CuAl₂ precipitates as compared with Figs. 11 and 12. Instead, the microstructure was similar to that of

a decrease in FSW torque or in the microstructure. A reduction in the volume fraction of the θ phase accompanied by a coarsening of the θ' phase cannot be explained by equilibrium kinetics, which would predict the dissolution of the smaller particles and coarsening of the larger particles within a constant temperature field.

Table 4 summarizes the bulk eddy current measurements. Similar readings were obtained for the 150 and 200 rev/min specimens, whereas the 300 rev/min specimen was significantly lower. It has been reported that the hardness does not have a 1-to-1 correlation with electrical conductivity in heat-treatable alloys (Ref. 45). At sufficiently high temperatures, dissolution of particles increased the amount of solid-solution solute causing a decrease in electrical conductivity. The increased solute presence results in natural aging of the weld nugget postweld thereby increasing the hardness. This hardness reversion with decreased electrical conductivity has been reported in other 2xxx series aluminum alloys (Refs. 45, 58) similar to the findings in this study. Although the combined use of eddy current and hardness testing was not generally used for identification of 2xxx series aluminum alloys (Ref. 45), it was useful for understanding the precipi-

tate state in the difference zones of a FSWs by correlation with complementary microscale techniques.

To further probe the bulk eddy current measurements, corresponding nanocurrent density measurements were calculated from indents applied in the center SZ region and the base metal region which was assumed to be near the edge of the transverse specimen. Figure 9 presents a bar graph plot showing the relative occurrence of each current density for the SZ (lighter color) and the base metal (darker color). At all rev/min conditions, a low occurrence of current densities in the range of 13–27 A/mm² is observed only in the SZ region. Comparing Fig. 9A and B, corresponding to the 150 and 200 rev/min specimens respectively, an increase can be observed in the occurrence of the current densities in the range of 11–21 A/mm². This increase in higher current densities for the 200 rev/min specimen corresponds to a decrease in the occurrence of the lower current densities (< 10 A/mm²). For the 300 rev/min specimen in Fig. 9C, the major occurrence of current densities is in the range of 1–5 A/mm² with similar behavior noted for the SZ and the base metal. Very few higher current densities in the SZ are observed in the narrower range 18–22 A/mm².

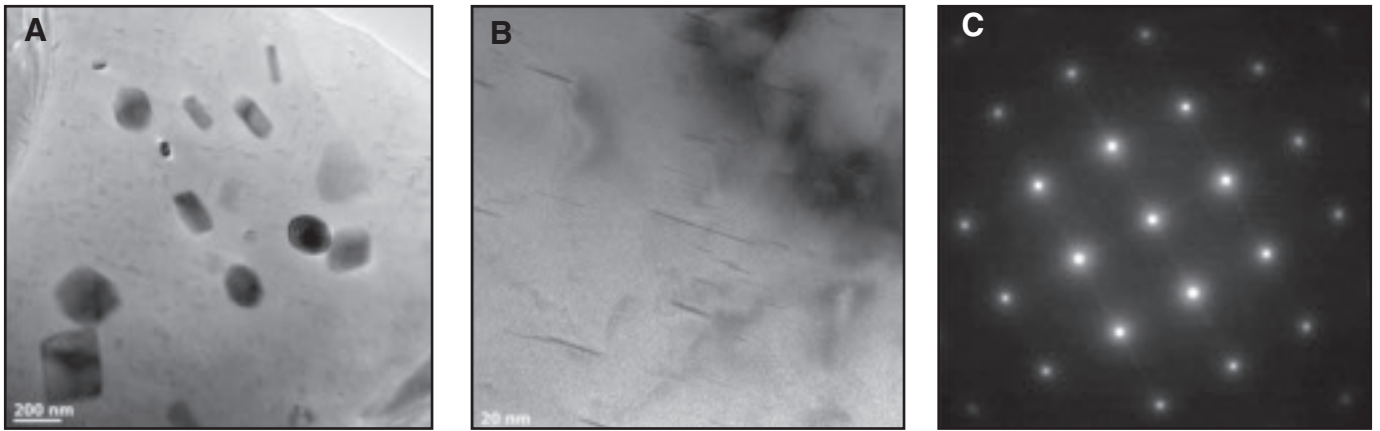


Fig. 11 — A and B — TEM images of the 150 rev/min FSW specimen; C — corresponding SAD pattern for the $[100]_{Al}$ zone axis of the aluminum matrix.

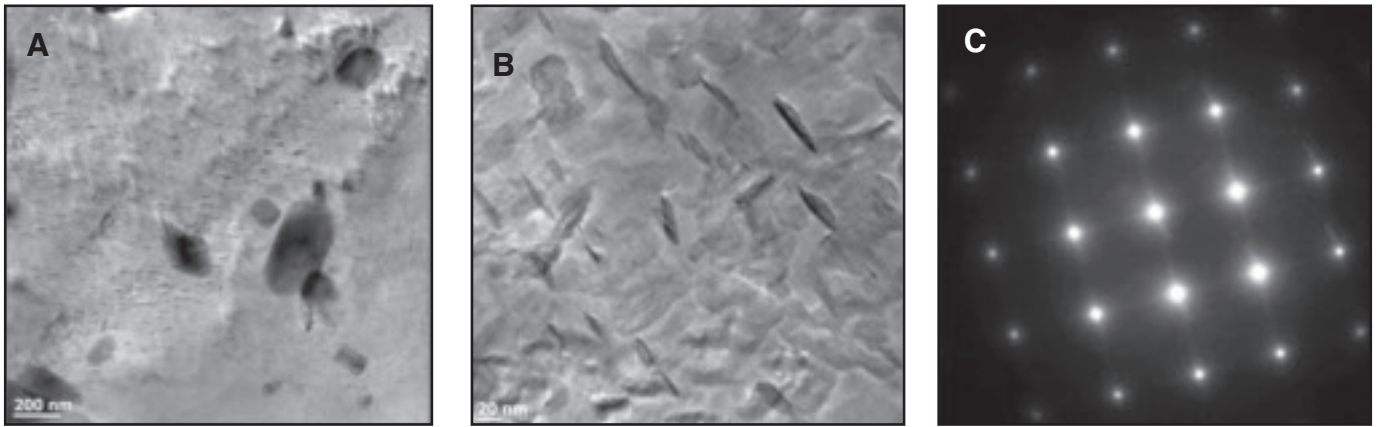


Fig. 12 — A and B — TEM images of the 200 rev/min FSW specimen; C — corresponding SAD pattern for the $[100]_{Al}$ zone axis of the aluminum matrix.

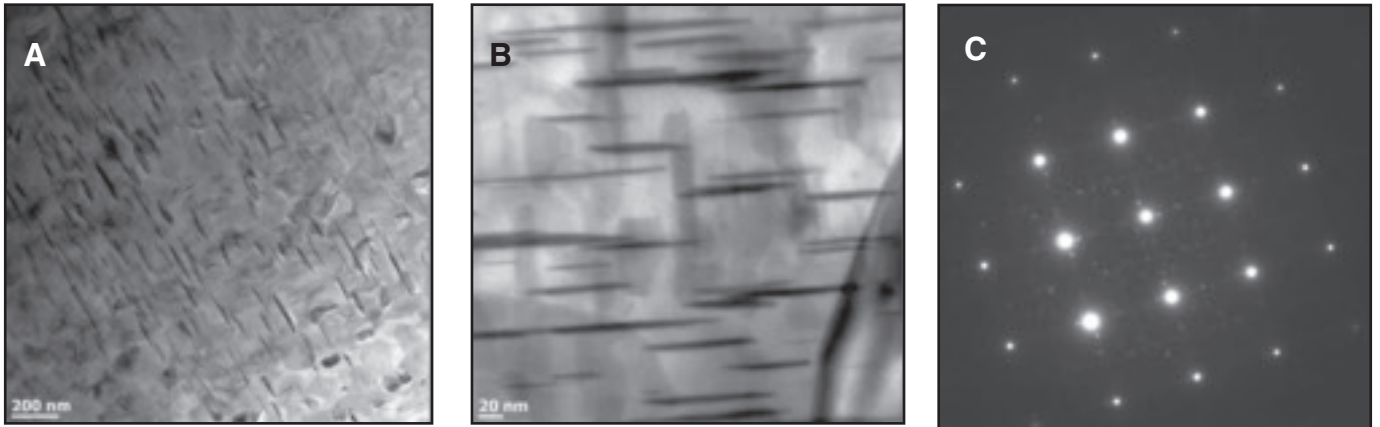


Fig. 13 — A and B — TEM images of the 300 rev/min FSW specimen; C — corresponding SAD pattern for the $[100]$ zone axis of the aluminum matrix. Note the superlattice reflections in the SAD pattern corresponding to the θ phase.

the base metal shown in Fig. 5.

To obtain a bulk characterization of the precipitate state in the FSW nugget, corresponding XRD analysis was also conducted. The XRD data are summarized in Fig. 14 with the minor peaks identified as the stable θ phase (Ref. 59). The θ phase peaks increased in intensity for the SZ of the 150 rev/min weld shown in Fig. 14B, decreased in intensity in Fig. 14C of the 200 rev/min weld, with further reductions in the 300 rev/min weld in Fig. 14D, which were similar in intensity to the base metal in Fig. 14A. This bulk XRD analysis was in agreement with the

TEM images in Figs. 11–13.

Using the torque data from the FSW panels, an alternative heat index (Ref. 27) was used to calculate the FSW temperatures as summarized in Table 5. The calculated temperatures ranged from 0.86–0.88 T_m , corresponding to the empirically published range of 0.80–0.90 T_m for FSW of AA2xxx alloys (Refs. 1, 2, 14–20). The phase diagram in Fig. 4 for Al-Cu binary system showed the nominal 6.30% Cu alloy was slightly above the maximum solid solubility composition. The α and θ phases can form a eutectic at a composition of 33.2 wt-% Cu with a eutectic temperature of 548°C. The

calculated temperatures were in agreement with experimental studies that showed an increase in peak temperature as the tool rotation increased. However, whether the small amount of temperature difference was responsible for the variations observed in the microstructure is questionable. Rather than a critical temperature threshold being crossed, it was proposed that only the material flow that crosses the severe shear zone into the SZ experiences heating rates that drive the stable θ phase into dissolution. Since a constant tool travel was maintained, the corresponding higher shear strain rate in addition to the higher tool rotation re-

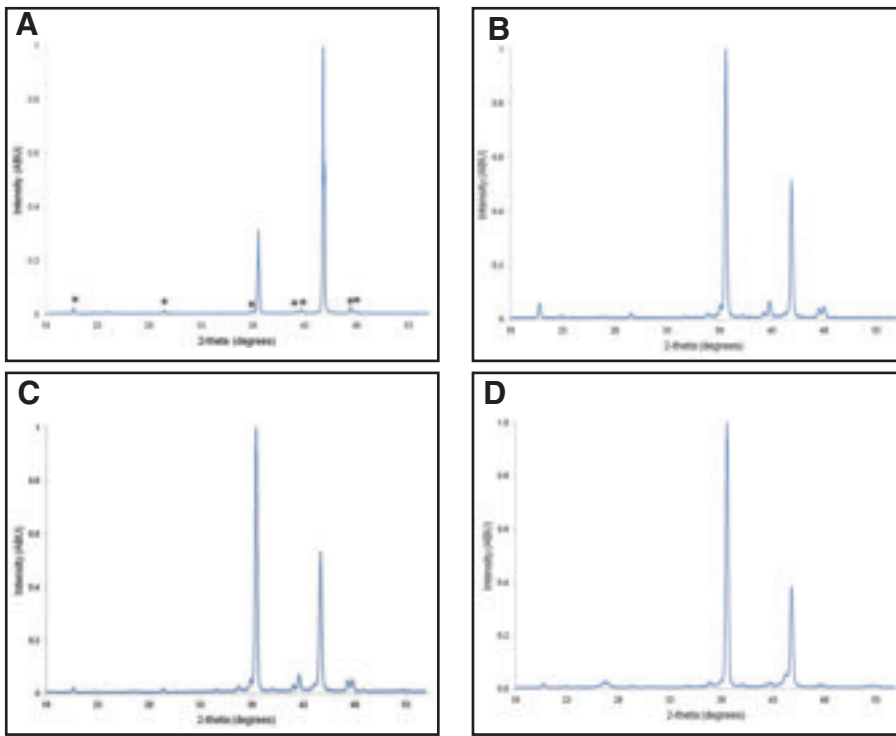


Fig. 14 — XRD results showing increasing presence of stable CuAl_2 precipitates from the base metal (A); to the 150 rev/min FSW (B). Intensity of the stable CuAl_2 decreases slightly in the 200 rev/min FSW (C); reverting to similar intensity as the base metal in the 300 rev/min FSW (D).

sulted in this material staying at temperature longer. Thus, the high heating rate increase combined with a longer time at temperature at 300 rev/min resulted in the θ dissolution that replenished the solute in the supersaturated α phase for postweld natural aging.

Based on the macro and micro scale data, the SZ of the FSW had a mixed state of stable and metastable Cu-rich phases. To obtain both dissolved larger particles and coarsened small particles implied that the material was subjected to two different temperature fields (Refs. 56, 57). This was explained using the kinematic model for FSW in which some material flow lines near the weld tool crossed a severe high shear rate region while other material flow lines further from the weld tool were subjected to lower shear rates and hence lower temperature (Refs. 11, 49, 56, 57).

Other researchers have observed decreased second phase particle size in the FSW microstructure corresponding with increased tool rev/min, which was attributed to fragmentation resulting from the shearing action of the material flow in the FSW process (Refs. 60, 61). Although agglomeration of θ particles have also been reported in a study at higher tool revs/min (Ref. 40), in addition to a study on second pass repair FSWs (Ref. 38).

The results in this study were consistent with another study on the microstructural evolution in AA2219-T87 (Ref. 15). Although that study (Ref. 15) only reported one set of unknown FSW parameters, sim-

ilar FSW strengths and precipitate state were reported that align with the results of the 200 rev/min specimen in this study. Correlation of microstructural evolution with the FSW temperature relied on the use of thermocouples mounted away from the SZ (Ref. 15). The measured temperature was extrapolated to the SZ resulting in an estimated value of 475°C or 0.8 T_m , which is lower than the 532°C or 0.86 T_m temperature calculated from the FSW data in this study for the shear zone.

Conclusions

In all the FSWs, a coarsening of the θ' phase was observed that resulted in the decreased SZ hardness and tensile strength. The solute lost from the α -matrix due to the coarsening of the θ' phases was eventually replaced by the dissolution of the θ phase at the higher tool rotation, which promoted postweld natural aging. Occurrence of coexisting coarsened θ' and θ phases in the SZ result from the combined effect of two flow streams of metal, which were subjected to different thermomechanical processing conditions. Thus, only the metal flow stream that crossed the severe shear zone experienced either higher temperatures or more severe shear as influenced by the tool rotation. At higher revs/min, the material also remains around the tool for a longer time, which suggests time at temperature was also critical to the final precipitate state.

Using the alternative heat indexing

method, the calculated temperature at 300 rev/min was estimated to be 542°C, which was close to the 548°C eutectic temperature shown on the Al-Cu phase diagram in Fig. 3. This provided a temperature rate sufficient for up-quenching to dissolve the θ phase in the FSW nugget region, but insufficient temperature to cause spontaneous melting of the θ phase. The resulting microstructure was similar to the base metal in conductivity as shown in Fig. 10 and hardness as shown in Fig. 8. While the calculated temperatures for the shear zone were not extreme over the range of FSW parameters investigated, they did highlight a region where critical changes in the microstructure in the SZ occurred. It was speculated that further increases in FSW rev/min may result in liquation as evidenced by a drop in weld power or torque. These FSWs were not performed as higher rev/min conditions in combination with the tool used in this study have resulted in voids.

The results of these experiments showed that processing parameters of FSW have a strong impact on precipitate position and dispersion, affecting localized mechanical and electrical properties. Due to the nonhomogeneity of the resulting FSW SZ, microscale hardness and conductivity measurements were useful in understanding the effect of precipitate state on the resulting electrical properties.

References

- Schmidt, H. B., and Hattel, J. H. 2005. A local model for the thermomechanical conditions in friction stir welding. *Modelling Simul. Mater. Sci. Engr.* 13: 77–93.
- Mishra, R. S., and Ma, Z. Y. 2005. Friction stir welding and processing. *Mat. Sci. & Engr.* R50: 1–78.
- Mendez, P. F., Tello, K. E., and Lienert, T. J. 2010. Scaling of coupled heat transfer and plastic deformation around the pin in friction stir welding. *Acta Mater.* 58: 6012–6026.
- Record, J. H., Covington, J. L., Nelson, T. W., Sorensen, C. D., and Webb, B. W. 2007. A look at statistical identification of critical process parameters in friction stir welding. *Welding Journal* 86(4): 97-s to 103-s.
- Lakshminarayanan, A. K., and Balasubramanian, V. 2008. Process parameters optimization for friction stir welding of RDE-40 aluminum alloy using Taguchi technique. *Trans. Nonferrous Met. Soc. China* 18: 548–554.
- Arora, K. S., Pandey, S., Schaper, M., and Kumar, R. 2010. Effect of process parameters on friction stir welding of aluminum alloy 2219-T87. *Int. J. Adv. Manuf. Technol.* 50: 941–952.
- Xu, W., Liu, J., Guohong, L., and Dong, C. 2009. Temperature evolution, microstructure and mechanical properties of friction stir welded thick 2219-O aluminum alloy joints. *Mat. & Design* 30: 1886–1893.
- Askari, A., Silling, S., London, B., and Mahoney, M. 2001. Modeling and analysis of friction stir welding process. *Friction Stir Welding & Processing*, ed. K. V. Jata, M. W. Mahoney, R. S. Mishra, S. L. Semiatin, and D. P. Field, pp. 43–54, TMS Pub.

9. Siedel, T. U., and Reynolds, A. P. 2003. Two-dimensional friction stir welding process model based on fluid mechanics. *Sci. & Tech. Welding & Joining* 8: 175–183.
10. Goetz, R. L., and Jata, K. V. 2001. Modeling friction stir welding of titanium and aluminum alloys. *Friction Stir Welding & Processing*, ed. K. V. Jata, M. W. Mahoney, R. S. Mishra, S. L. Semiatin, and D. P. Field, pp. 35–41, TMS Pub.
11. Nunes, A. C. Jr., 2012. The evolution of friction stir welding theory at Marshall Space Flight Center. *Proceedings of 9th Int'l Symp. FSWing*, Huntsville, Ala., TWI pub.
12. Jata, K. V., and Semiatin, S. L. 2000. Continuous dynamic recrystallization during friction stir welding. *Scripta Mater.* 43: 743–748.
13. Gerlich, A., Su, P., Yamamoto, M., and North, T. H. 2007. Effect of welding parameters on the strain rate and microstructure of friction stir spot welded 2024 aluminum alloy. *J. Mater. Sci.* 42: 5589–5601.
14. Subramanian, P. R., Nirmalan, N. V., Young, L. M., Sudkamp, P., Mika, D. P., Larsen, M., Othon, M. A., Dupree, P. L., Walker, S. O., and Catlin, G. M. 2003. Fundamental studies of microstructure evolution during stir welding of aluminum alloys. USAF/AFRL Final Report Grant F49620-01-1-0300.
15. Arora, K. S., Pandey, S., Schaper, M., and Kumar, R. 2010. Microstructure evolution during friction stir welding of aluminum alloy AA2219. *J. Mater. Sci. Technol.* 26: 747–753.
16. Chao, Y. J., Qi, X., and Tang, W. 2003. Heat transfer in friction stir welding — Experimental and numerical studies. *Trans. ASME* 125: 138–145.
17. Heurtier, P., Jones, M. J., Desrayaud, C., Driver, J. H., Montheillet, F., and Allehaux, D. 2006. Mechanical and thermal modeling of friction stir welding. *J. Mat. Proc. Tech.* 171: 348–357.
18. Vilaca, P., Quintino, L., dos Santos, J. F., Zettler, R., and Sheikh, S. 2007. Quality assessment of friction stir welding joints via an analytical thermal model, iSTIR. *Mat. Sci. & Engr.* A445-446: 501–508.
19. Genevois, C., Fabregue, D., Deschamps, A., and Poole, W. J. 2006. On the coupling between precipitation and plastic deformation in relation with friction stir welding of AA2024-T3 aluminium alloy. *Mat. Sci. & Engr.* 441A: 39–48.
20. Chen, Y. C., Feng, J. C., and Liu, H. J. 2009. Precipitate evolution in friction stir welding of 2219-T6 aluminum alloys. *Mat. Charact.* 60: 476–481.
21. Colegrove, P. A., and Shercliff, H. R. 2004. Two-dimensional CFD modeling of flow round profiled FSW tooling. *Sci. & Tech. Welding & Joining* 9: 483–492.
22. Colegrove, P. A., and Shercliff, H. R. 2005. 3-Dimensional CFD modeling of flow round a threaded friction stir welding tool profile. *J. Mat. Proc. Tech.* 169: 320–327.
23. Khandkar, M. Z. H., Khan, J. A., and Reynolds, A. P. 2003. Prediction of temperature distribution and thermal history during friction stir welding: input torque based model. *Sci. & Tech. Welding & Joining* 8: 165–174.
24. El-Domiati, A., and El-hafez, H. A. 2007. An energy model for friction stir welding. *Materials Science and Technology (MS&T) Conf. Proc.*, Detroit, Mich., pp. 435–447.
25. Pew, J. W., Nelson, T. W., and Sorensen, C. D. 2007. Development of a torque-based weld power model for friction stir welding. *Friction Stir Welding & Processing IV*, ed. R. S. Mishra, M. W. Mahoney, T. J. Lienert, and K. V. Jata, pp. 73–81, TMS Pub.
26. Arora, A., Nandan, R., Reynolds, A. P., and DebRoy, T. 2009. Torque, power requirement and stir zone geometry in friction stir welding through modeling and experiments. *Scripta Mater.* 60: 13–16.
27. Querin, J. A., and Schneider, J. A. 2012. Developing an alternative heat indexing equation for FSW. *Welding Journal* 91: 76-s to 82-s.
28. Frigaard, O., Grong, O., and Midling, O. T. 2001. A process model for friction stir welding of age hardenable aluminum alloys. *Met. Trans.* 32A: 1189–1200.
29. Strangwood, M., Berry, J. E., Cleugh, D. P., Leonard, A. J., and Threadgill, P. L. 1999. Characterization of the thermomechanical effects on microstructural development in friction stir welded age hardening aluminum-based alloys. *1st Int'l Symp. FSW*, Thousand Oaks, Calif., TWI Pub.
30. Murr, L. E., Li, Y., Trillo, E. A., Nowak, B. M., and McClure, J. C. 1999. A comparative study of friction stir welding of aluminum alloys. *Al. Trans.* 1(1): 141–154.
31. Li, Z. X., Arbogast, W. J., Hartley, P. J., and Meletis, E. I. 1999. Microstructure characterization and stress corrosion evaluation of friction stir welded Al 2195 and Al 2219 alloys. *Proc. 5th Intl. Conf. on Trends in Welding Res.* pp. 568–573, AWS pub.
32. Litynska, L., Braun, R., Staniek, G., Dalle Donne, C., and Dutkiewicza, J. 2003. TEM study of the microstructure evolution in a friction stir welded AlCuMgAg alloy. *Mat. Chem. & Physics* 81:293–295.
33. Genevois, C., Deschamps, A., Denquin, A., and Doisneau-Cottignies, B. 2005. Quantitative investigation of precipitation and mechanical behavior for AA2024 friction stir welds. *Acta Mater.* 53: 2447–2458.
34. Jones, M. J., Heurtier, P., Desrayaud, C., Montheillet, F., Allehaux, D., and Driver, J. H. 2005. Correlation between microstructure and microhardness in a friction stir welded 2024 aluminium alloy. *Scripta Mater.* 52: 693–697.
35. Barcellona, A., Buffa, G., Fratini, L., and Palmeri, D. 2006. On microstructural phenomena occurring in friction stir welding of aluminium alloys. *J. Mat. Proc. Tech.* 177: 340–343.
36. Chen, Y., Liu, H., and Feng, J. 2006. Friction stir welding characteristics of different heat treated state 2219 aluminum alloy plates. *Mat. Sci. & Engr.* A. 420: 21–25.
37. Paglia, C. S., and Buchheit, R. G. 2006. Microstructure, microchemistry and environmental cracking susceptibility of friction stir welded 2219-T87. *Mat. Sci. & Engr.* 429A: 107–114.
38. Li, B., and Shen, Y. 2011. The investigation of abnormal particle-coarsening phenomena in friction stir repair weld of 2219-T6 aluminum alloy. *Mat. & Design* 32: 3796–3802.
39. Fonda, R. W., Knipling, K. E., and Bingert, and J. F. 2007. Microstructural evolution ahead of the tool in aluminum friction stir welds. *Scripta Mater.* 58: 343–348.
40. Cao, G., and Kou, S. 2005. Friction stir welding of 2219 aluminum: Behavior of (Al₂Cu) particles. *Welding Journal* 84(1): 1-s to 8-s.
41. Sutton, M. A., Yang, B., Reynolds, A. P., and Taylor, R. 2002. Microstructural studies of friction stir welds in 2024-T3 aluminum. *Mat. Sci. & Engr.* A323: 160–166.
42. Yang, B., Yan, J., Sutton, M. A., and Reynolds, A. P. 2004. Banded microstructure in AA2024-T351 and AA2524-T351 aluminum friction stir welds: Part I Metallurgical studies. *Mat. Sci. & Engr.* A364: 55–65.
43. Van Drunen, G., and Cecco, V. S. 1984. Recognizing limitations in eddy current testing. *NDT Int'l* 17: 9–17.
44. Blitz, J. 1987. Eddy current testing of metals. *Mats. & Design* 8: 340–345.
45. Lee, E. W., Oppenheim, T., Robinson, K., Aridkahari, B., Neylan, N., Gebreyesus, D., Richardson, M., Arzate, M., Bove, C., Iskandar, M., Sanchez, C., Toss, E., Martinez, I., Arenas, D., Ogren, J., McLennan, J., Clark, R., Frazier, W. E., and Es-Said, O. S. 2007. The effect of thermal exposure on the electrical conductivity and static mechanical behavior of several age hardenable aluminum alloys. *Engr. Failure Analysis* 14: 1538–1549.
46. Davis, A. M. 2010. Interaction of the friction stir welding tool and workpiece as influenced by process parameters in friction stir welding. MS Thesis, Mississippi State University.
47. IACS standard, 1914. *International Standard of Resistance for Copper*, International Electrotechnical Commission, Publication 28.
48. ASTM E8/E8M-09, *Standard Test Methods for Tension Testing of Metallic Materials*. 2003. ASTM Int'l, West Conshohocken, Pa. DOI:10.1520/E0008_E0008M-09, www.astm.org.
49. Nunes, A. C. Jr. 2001. Wiping metal transfer in friction stir welding. *Aluminum 2001, Proc. TMS Annual Mtg*, pp. 235–248.
50. *Metals Handbook*. 1990. Vol. 2: Properties and Selection: Nonferrous Alloys and Special-Purpose Materials, 10th ed., pp. 81. ASM Pub., Materials Park, Ohio.
51. *Metals Handbook*. 1973. Vol. 8: Metallography, Structures, and Phase Diagrams, 8th ed., pp. 259. ASM pub., Materials Park, Ohio.
52. *Metals Handbook*. 1991. Vol. 4: Heat Treating, pp. 845–845. ASM pub., Materials Park, Ohio.
53. Wang, S. C., and Starink, M. J. 2005. Precipitates and intermetallic phases in precipitation hardening Al-Cu-Mg-(Li) based alloys. *Int. Mater. Rev.* 50: 193–215.
54. Huang, C., and Kou, S. 2004. Liquation cracking in full penetration Al-Cu welds. *Welding Journal* 82(2): 50-s to 58-s.
55. Su, J.-Q., Nelson, T. W., and Sterling, C. J. 2005. Microstructural evolution during FSW/FSP of high-strength aluminum alloys. *Mat. Sci. & Engr.* 405A: 277–286.
56. Schneider, J. A., Nunes, A. C. Jr., Chen, P. S., and Steele, G. 2005. TEM study of the FSW nugget in AA2195-T81. *J. Mat. Sci.* 40: 4341–4345.
57. Schneider, J. A., and Nunes, A. C. Jr., 2004. Characterization of plastic flow and resulting micro textures in a friction stir weld. *Met. Trans.* B35: 777–783.
58. Rosen, M., Horowitz, E., Swartzendruber, L., Fick, S., and Mehrabian, R. 1982. The aging process in aluminum alloy 2024 studies by means of eddy currents. *Mat. Sci. & Engr.* 53: 191–198.
59. International Center for Diffraction Data (ICDD) Powder diffraction file (PDF) file # 015-1372 for Al₂Cu (θ phase).
60. Attallah, M. M., and Salem, H. G. 2005. Friction stir welding parameters: a tool for controlling abnormal grain growth during subsequent heat treatment. *Mat. Sci. & Engr.* A391: 51–59.
61. Fonda, R. W., and Lambrakos, S. G. 2002. Analysis of friction stir welds using an inverse problem approach. *Sci. & Tech. Weld & Joining* 7: 177–181.